Combined Experimental and Numerical Study of the Free Vibration of Surface-Piercing Struts

Casey Harwood, Andrew Stankovich, Yin Lu Young, Steven Ceccio

Combined Experimental and Numerical Study of the Free Vibration of Surface-Piercing Struts

Casey M. Harwood[1]*, Andrew J. Stankovich[2], Yin Lu Young[1], Steven L. Ceccio[1,3]

ISROMAC 2016

International Symposium on Transport Phenomena and Dynamics of Rotating Machinery

Hawaii, Honolulu

April 10-15, 2016

Abstract

Experiments and simulations were performed on surface-piercing struts constructed of aluminum and PVC to investigate the effects of partial-immersion and multi-phase flow on the modes of free-vibration. Experiments were conducted with the struts suspended in a water-filled drum and excited with hammer-strikes. A shape-sensing methodology was used to experimentally infer mode shapes of the PVC strut. The finite element method (FEM) model used acoustic elements to simulate the fluid domain. Resonant frequencies generally decreased as immersion depth increased as a result of increasing hydrodynamic added mass. The percentage-change in resonant frequencies varied between modes. The first bending mode was the most strongly affected by partial immersion, while the first lead-lag mode was almost unaffected. The second and third resonant frequencies were observed to coalesce or change order for the aluminum and PVC struts, respectively; both cases highlight the possibility of dangerous energy-exchange between modes. Atmospheric ventilation was simulated in the FEM model by using acoustic air elements to represent a ventilated cavity along the suction-surface of each strut. Ventilation reduced the added mass, causing resonant frequencies to increase to values between the fully-wetted and *in-vacuo* frequencies.

Keywords

Ventilation – Vibration – Surface-Piercing – Struts – Hydrofoils

[1] *Department of Naval Architecture and Marine Engineering, University of Michigan, Ann Arbor, MI, USA*

[2] *Altair Engineering, Troy, MI, USA*

[3] *Department of Mechanical Engineering, University of Michigan, Ann Arbor, MI, USA*

*__Corresponding author__: cmharwoo@umich.edu

INTRODUCTION

Many high-lift devices operate in a surface-piercing configuration, including surface-piercing propellers, hydrofoils, rudders, and control surfaces. Other systems, like supercavitating propellers, dynamic positing thrusters, and submerged hydrofoils operate in close proximity to the free surface. Both cases present an increased risk of atmospheric ventilation (the entrainment of an air-filled cavity).

Additionally, recent moves toward flexible marine structures - both in research and in industry - have revealed the potential for hydro-elastic instabilities that are not adequately predicted by classical aero-elastic theory [1, 2, 3, 4]. Ventilated flow around a flexible hydrofoil/strut presents an extremely complicated hydro-elastic problem. The interface between a very light fluid (air) and a very dense fluid (water) creates dramatic spatial and temporal variations in the pressure and density fields surrounding a surface-piercing body. The ramifications on the effective system added mass, damping, stiffness, and resonant properties are unknown. In this work, combined experimental and numerical studies are performed to measure the hydro-elastic response of surface-piercing struts in wetted and ventilated flows.

BACKGROUND

The issue of atmospheric ventilation on surface-piercing bodies has been investigated by [5, 6], among others. Recently, [7, 8] performed towing-tank experiments on a surface-piercing strut constructed of aluminum. They established characteristic flow regimes, which include fully-wetted (FW) and fully-ventilated (FV) flows, depicted in Figure 1. The flows present dramatically-different distributions of high- and low-density fluid surrounding the body; the transitions between flow regimes can be violent, inducing large load-fluctuations.

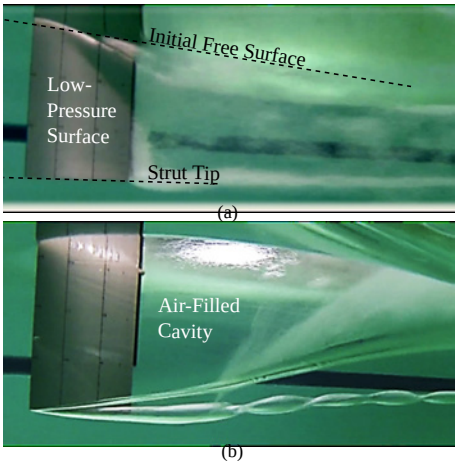

Figure 1. (a) Fully-wetted (FW) regime, where the suction surface of the yawed strut (pictured) is completely wetted. **(b)** Fully-ventilated (FV) flow, where a cavity of atmospheric air is entrained around the suction surface of the yawed strut.

Past research on the partial-immersion of elastic structures have been mostly limited to fully-wetted flows around bodies with simple circular or rectangular cross sections. [9] used a combined finite-element-method-boundary-element-method (FEM-BEM) model to investigate the natural and resonant

modes of a flat surface-piercing plate. For partially-immersed, fully-wetted cases, a boundary-value problem was established on the fluid-domain to emulate a linear free surface and infinite fluid field, and the plate was discretized with singularity panel distribution. The *in-vacuo* mode shapes were determined with the FEM model and used to decouple the equations of motion. Using the pre-computed mode shapes as effective basis functions, the solution to the generalized equation of motion allowed resonant frequencies, ω, principal (modal) coordinates, and modal added mass and damping coefficients to be obtained. They found that the free surface induced a frequency-dependence into the modal added mass and damping – a consequence of the radiation potential. The frequency-dependence vanished quickly with both increasing immersion depth and increasing modal frequency. Variations in the added mass, in particular, were only appreciable for values of $\omega\sqrt{S/g} < 5$, where S is the span of the plate and g is gravitational acceleration.

[10] presented an analysis of metallic and composite cantilevered plates, both in-water and in-vacuum, using combined numerical and analytical methods. The work showed good agreement with experimental measurements of a cantilevered surface-piercing steel plate provided in [11]. The wetted frequencies were found to be much lower than the dry frequencies as a result of fluid inertial effects (added mass). The percentage reduction in resonant frequencies (compared to the dry state) varied between modes. Moreover, the changes in wet-to-dry frequency ratios were more severe for lightweight models than for heavier models. Results showed that added mass, and therefore wetted frequency, were strongly dependent on the respective mode shapes, which in turn are determined by the body shape, support-type, physical properties, and material anisotropy. Similarly, [12] used finite element analysis to show that there is a significant reduction in resonance frequency as the immersion-depth of the plates increased, due to larger fluid added mass, and that these effects are dependent on the particular shape of the resonance mode. The results showed that as the submergence increased, the resonance frequencies decreased, asymptotically approaching the frequencies for a fully-submerged plate.

Objectives

The objective of this work is to improve the understanding of the hydro-elastic behavior of surface-piercing struts to assist in future design and control of struts and hydrofoils across a variety of operating conditions. Specifically, this study seeks to investigate the effects of partial immersion and ventilated flow on the resonant frequencies, added mass, and associated mode shapes of surface-piercing struts through combined experimental and numerical analyses. Moreover, this study aims to develop and validate a numerical approach for the simulation of wetted and ventilated surface-piercing bodies.

1. EXPERIMENTAL APPROACH

Geometrically-identical struts were constructed from aluminum and PVC, using the geometry of [7, 8]. The design

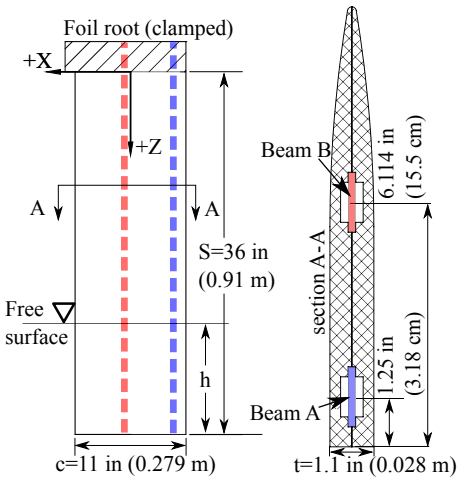

Figure 2. The geometry of the struts. The aluminum and PVC struts both possess a semi-ogival section. The aluminum strut is solid. The PVC strut includes two interior channels, into which are installed shape-sensing spars (Figure 3).

possesses a semi-ogival section with a circular-arc fore-body and rectangular after-body, as shown in Figure 2. The aluminum strut was machined with a solid section. The PVC strut was constructed from two symmetric halves, which were affixed by a chemical bond and plastic-welding. Along the centerline of the PVC strut, two interior channels were machined, into which custom-built shape-sensing spars were installed.

Inferring motions of flexible structures typically requires accelerometry and/or optical methods. The former poses problems for non-harmonic motions, while the latter cannot operate in environments where fluid interfaces cause refraction (such as in the case of a ventilated cavity). A non-optical means of tracking structural deflections was developed in the form of shape-sensing spars, pictured in Figure 3.

The shape-sensing methodology invokes the beam bending equation,

$$\epsilon_z \approx \frac{-t}{2}\frac{\partial^2 Y}{\partial Z}, \tag{1}$$

where ϵ_z is the surface bending strain on a beam of thickness t, Y is the coordinate in the direction of lateral beam deflection

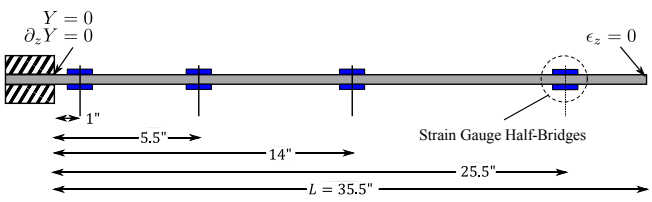

Figure 3. A schematic illustration of the shape-sensing spar. Strain gauges permit the distribution of strain along the beam to be approximated via polynomial, from which the deflection may be inferred. Two identical spars were constructed and inserted into the PVC strut at locations indicated by the blue and red regions in Figure 2.

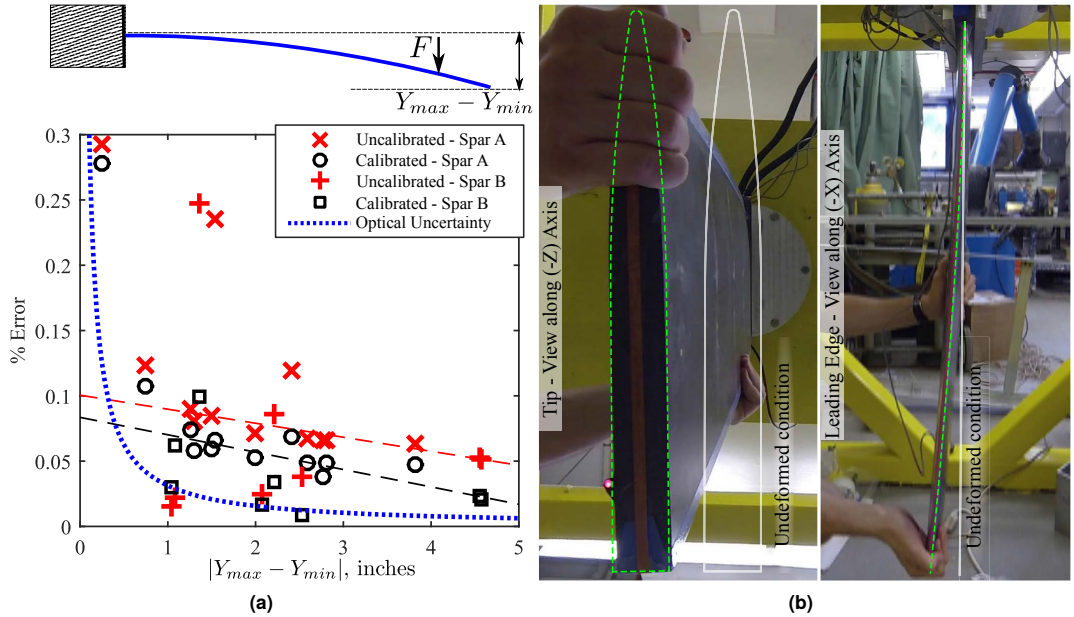

Figure 4. **(a)** The loading condition under which errors were measured (single concentrated loads at varying spanwise locations) and the maximum percentage error for the individual spars (A and B). The errors are significantly reduced by the calibration step, and are bounded below by the propagated uncertainty in the optically-measured deflections. **(b)** The (post-calibration) tip-deflection and the leading edge deflection inferred from the pair of shape-sensing spars are overlaid as green dashed lines onto photos of the strut subjected to a combined bending/twisting load. A compliance factor of $\kappa = 8$ was used to relax the root boundary conditions. White solid lines indicate the initial undeformed geometry of the strut's tip and leading edge.

and Z is the coordinate along the initial (undeformed) length of the beam. The slim aluminum spar is instrumented with N strain gauges in a half-cosine spacing. The boundary condition, $\epsilon_z|_{Z=L} = 0$, permits an N^{th}-order polynomial may be fitted to the measured strains.

$$\hat{\epsilon_z}(Z) = \sum_{i=0}^{N} a_i Z^i. \tag{2}$$

EQ 2 may be substituted into EQ 1 and twice-integrated to yield a polynomial approximation of the lateral deflection.

$$\hat{Y}(Z) = \sum_{0}^{N+2} A_i Z^i. \tag{3}$$

The integration yields two additional coefficients, A_0 and A_1, which must be determined from the beam's boundary conditions. For an ideal cantilever, $A_0 = A_1 = 0$, giving

$$A_i = \begin{cases} 0, & j = 0, 1 \\ \dfrac{a_i (j-2)!}{j!}, & j = 1, 2, \ldots, N+2 \end{cases}$$

Two spars were constructed, denoted "A" and "B". Independent optical calibrations were carried out to correct for small differences in the strain-gauge mounting, such as orientation, adhesive thickness, and other linearizable sources of variation. The root of the spar was clamped and point loads were applied to the beam to achieve various static deflections. A calibrated camera was used to measure the lengthwise deflections with an estimated uncertainty of 1/32 in (0.79 mm), from which the surface strains were calculated *via* EQ 1. A calibration matrix, unique to each spar, was fitted to minimize the squared error between the strain values measured optically and those measured by the strain gauges. The error of the pre- and post-calibration deformations is plotted in Figure 4a. The plotted symbols, and the linear trends fitted to them, make it clear that the calibration significantly reduced both the mean error and the variance of the error.

Under the assumption that bending along the chord is negligible (chord-wise rigidity), the deflections along the two spars – respectively $\hat{Y_A}(Z)$ and $\hat{Y_B}(Z)$ – may be used to reconstruct the deformed centerline plane of the strut. It is convenient to recast the deformations into the decoupled angular and lateral deflection of each spanwise section along the elastic axis.

$$\hat{\theta}(Z) = \arctan\left(\frac{\hat{Y_A}(Z) - \hat{Y_B}(Z)}{X_A - X_B}\right) \tag{4a}$$

$$\hat{Y_{EA}}(Z) = \hat{Y_A}(Z) + (X_{EA} - X_A)\tan(\theta(Z)), \tag{4b}$$

where X_A and X_B respectively denote the chordwise positions of the spars inside of the strut and X_{EA} denotes the chordwise location of the elastic axis.

In practice, the root of each spar was judged to be imperfectly clamped as a result of the compliance of the surrounding PVC, such that $Y(Z) = 0$ but $Y'(Z) \neq 0$ at $Z = 0$. The coefficient A_1 in EQ 3 was changed to $A_1 = -\kappa\hat{\epsilon_z}|_{Z=0}$, where

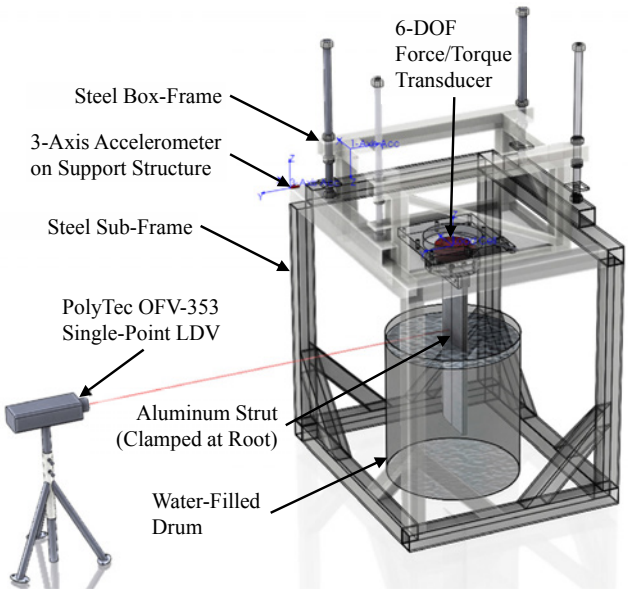

Figure 5. Experimental setup used to measure vibratory response of struts. A large steel structure holds the surface-piercing strut in a vertically-cantilevered configuration, suspended either in air or in a 65-gallon (246 liter) drum with the free tip immersed to depth h.

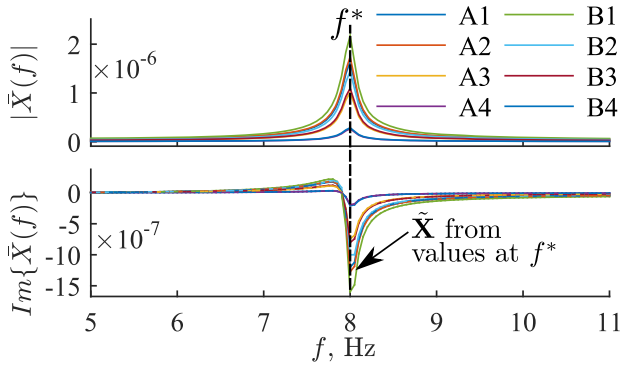

Figure 6. The magnitude and imaginary parts of the strain-gauge signals in the frequency domain. The first resonant mode is shown ($f_1^* = 8$ Hz), indicated by the peaked response magnitude. The operating deflection shape (ODS) strains are obtained from the crossing of imaginary parts of the strain-gauge signals with f_1^*. The legend entries are the numbered strain gauges on spars A and B ($N_{A,B} = 4; N = 8$).

κ represents a dimensionless compliance factor, allowing the root of each spar to take on a non-zero slope proportional to the applied moment at $Z = 0$, and which must be determined *in-situ*. An example of the inferred bending/twisting deformation of the strut under the relaxed boundary condition ($\kappa = 8$) is shown in Figure 4b. The inferred deflections are overlaid onto calibrated photos of the strut's tip and leading edge in green dashed lines. Good agreement between the inferred and true deformations may be observed.

To collect vibration data, each strut was suspended from a steel carrier in a vertical cantilevered configuration. The root of the strut was clamped and coupled to the steel structure via a six-degree-of-freedom load cell. The free tip of the strut was lowered into a 65-gallon (246 liter drum). The drum was filled with freshwater until the desired depth of immersion (h) was achieved. Immersed aspect ratios ($AR_h = h/c$) of 0, 0.5, 1.0, and 1.5 were assessed, with $AR_h = 0$ corresponding to the dry configuration. The motions of the strut were measured via a Polytec OFV-353 single-point laser doppler velocimeter (LDV) and – in the case of the PVC strut only – the internal shape-sensing spars. Finally, a three-axis accelerometer was attached to sub-frame to measure the vibratory response of the test structure. The strut was excited by hammer strikes, after which the decaying free-vibration response was recorded as a time-series of length M. Sampling rates of $F_s = 1$ kHz and 5 kHz were used for the aluminum and PVC struts, respectively. The experimental setup is illustrated in Figure 5.

Discrete Fourier transforms (DFT) were used to generate frequency spectra for each recorded channel,

$$\bar{\boldsymbol{X}} = \mathcal{D}(\boldsymbol{X}), \tag{5}$$

where $\boldsymbol{X}$ is the time-series of of sampled data at times $\boldsymbol{t} = \{t_n, n = 1, 2, \ldots, M\}$. $\bar{\boldsymbol{X}}$ is a complex-valued vector corresponding to frequencies $\boldsymbol{f} = \{ f_n, n = 1, 2, \ldots, M\}$. The magnitudes of the frequency response $|\bar{\boldsymbol{X}}|$ were plotted for each collected data channel, denoted by index j, and the collective frequency distributions were used to locate peaks in the frequency spectra corresponding to resonant modes (see Figure 6). The location of the peak on each channel was taken as the j^{th} estimate of the resonant frequency, $f_{i,j}^*$, where i is the ordered mode number.

Taking the imaginary part of $\bar{\boldsymbol{X}}_n$ at a frequency yields the operating deflection shape (ODS) for frequency f_n. When the sampled strain-gauge signals are considered, the ODS is an estimate of the strain distribution, $\boldsymbol{\epsilon_z} = \left\{\epsilon_{z_j}, j = 1 \ldots N\right\}$, that oscillates sinusoidally at that frequency.

$$\tilde{\boldsymbol{\epsilon_z}} \approx \tilde{\boldsymbol{X}}_n = \text{Im}(\bar{\boldsymbol{X}}_n), \tag{6}$$

The ODS strains for each resonant condition were translated into a surface ODS ($\tilde{\boldsymbol{Y}}$) *via* EQs 2-4. For resonant peaks that are well-separated, the surface ODS is dominated by the underlying normal mode shape, $\boldsymbol{\Phi}$ [13].

$$\tilde{\boldsymbol{Y}}_n \approx \boldsymbol{\Phi}_i \qquad \text{when} \qquad f_n = f_{i,j}^* \tag{7}$$

The strain-gauge channels ($j = 1 \ldots N$) were each considered, yielding N estimates of each resonant frequency and associated ODS. Moreover, eight-to-twelve trials were conducted per value of AR_h, permitting the mean and standard deviations of the resonant frequencies and ODSs to be estimated. Figure 6 shows the averaged frequency response of the strain-gauge signals at $AR_h = 0$ in the neighborhood of the first resonant frequency. The top plot shows the magnitude of the frequency response, with a vertical line indicating the resonant peak. The imaginary part of the frequency-response is shown in the lower plot; the ODS strains are recorded as the set of values intersecting the vertical bar.

Table 1. The geometric properties of the strut, which are identical for the PVC and aluminum struts, and the masses, which vary with the strut material. Quantities exclude the root-portion of each strut.

Property	$\mathbf{I}_{xx}$ in^4 (m^4)	$\mathbf{I}_{yy}$ in^4 (m^4)	**J** in^4 (m^4)	m_{AL} slugs (kg)	m_{PVC} slugs (kg)
Value	0.92 (3.829×10^{-7})	86.99 (3.621×10^{-5})	87.9 (3.659×10^{-5})	1.14 (16.61)	0.56 (8.19)

Table 2. The material properties of the PVC and aluminum struts and the fluid used in the FEM analysis.

Material	**Mass Density** lbf s^2/in^4 (kg/m^3)	**Young's Modulus** psi (GPa)	**Poisson Ratio**	**Bulk Modulus** psi (GPa)
Aluminum	2.53×10^{-4} (2700)	1.00×10^{7} (8.94)	0.33	9.80×10^{6} (67.57)
PVC	1.22×10^{-4} (1330)	4.00×10^{5} (2.76)	0.4	6.67×10^{5} (3.91)
Water	9.36×10^{-5} (1000)	-	-	3.19×10^{5} (2.20)
Air	1.15×10^{-7} (1.23)	-	-	20.59 (1.42×10^{-4})

1.1 Numerical Approach

The commercial finite element software, Abaqus, was used to analyze the first five resonant frequencies of the strut structure in the frequency domain. The Lanczos solver was used to extract the coupled structural-acoustic resonant frequencies [14].

The geometric properties of the struts (excluding the clamped root) are listed in Table 1 and material properties of the two different struts and the acoustically modeled fluid domain are listed in Table 2. The second moments of area, I_{xx}, I_{yy}, and J (Z-axis Rotation), are shown in the table as well as the mass m of the aluminum (AL) and PVC struts.

The strut was meshed using 3-D reduced integration, first order continuum shell elements (SC8R) [14] following the success shown in [10]. The meshed strut is shown in Figure 7a with (n_x, n_y, n_z) indicating the number of elements in each coordinate direction. The origin of the strut is specified at the intersection of the mid-chord plane, centerline plane, and strut root ($Z = 0$) plane. The fluid domain was modeled as a radial projection of the strut cross section. 3-D first-order, reduced integration acoustic elements (AC3D8R) [14] were chosen for the fluid, again based on the findings of [10]. To simulate ventilation, air properties were applied to a region of the acoustic fluid domain (shown in Figure 7b).

Convergence studies were performed sequentially, first refining the solid mesh and then determining the fluid domain size. The solid mesh was considered converged when further refinement on $n_{z,y,z}$ yielded changes in the first resonant frequency of less than 0.5%. The dimensions of the fluid domain were varied next (the fluid mesh size is defined by the converged solid mesh), and the first resonant frequency was again judged to be converged when further increases to the domain size yielded changes of less than 0.5%. The converged solid mesh parameters and fluid domain size are given in table 3.

1.2 Boundary Conditions

All degrees of freedom were fixed on the nodes of the strut's root to simulate the cantilevered test configuration. The kinematic/dynamic free surface boundary condition for potential

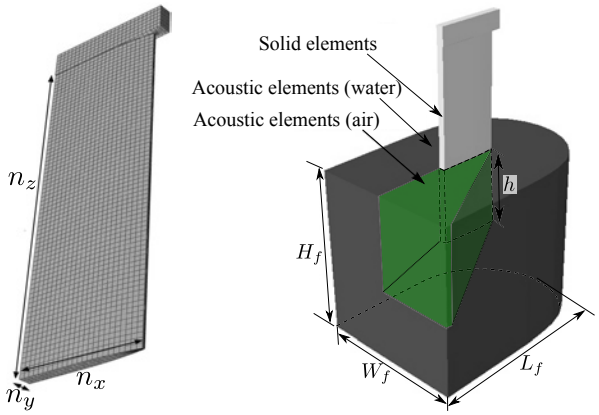

(a) Strut mesh **(b)** Domain size

Figure 7. (a) The FEM mesh parameters of the surface-piercing strut. **(b)** The dimensional parameters of the fluid domain. FW and FV flows were simulated by respectively specifying the green region as water or air acoustic elements.

(inviscid and irrotational) flow is,

$$\partial^2\phi/\partial t^2 + g\partial\phi/\partial z = 0 \tag{8}$$

with the velocity potential, ϕ, defined as,

$$\phi(x, y, z, t) = \phi_o \cdot e^{(i(\boldsymbol{kr}-\omega t))} \tag{9}$$

where ϕ_o is the complex amplitude, $\boldsymbol{k}$ is the wave-vector, ω is the angular frequency, and $\boldsymbol{r}$ is the position vector (x, y, z).

Table 3. Converged parameters of solid mesh and fluid domain, as defined in Figure 7 (strut dimensions are shown in Figure 2).

Solid Mesh		Fluid Domain	
n_x	24	L_f, in (m)	37.5 (0.953)
n_y	10	W_f, in (m)	25.85 (0.657)
n_z	72	H_f, in (m)	28.88 (0.734)
# Elements	21,600	# Elements	406,428

When EQ 9 is evaluated at very high frequencies it can be reduced to show that

$$\lim_{\omega\to\infty} \phi(x, y, z, t) = 0. \tag{10}$$

This approximation is only strictly valid at high frequencies, as $\omega \to \infty$. However, as shown in [9], the boundary condition was found to be approximately valid for $\omega\sqrt{S/g} > 5$. In the present work, dimensionless modal frequencies were found to satisfy this condition in all cases, so EQ 10 was judged to be a suitable boundary condition. Non-reflecting boundary conditions were imposed on the bottom and sides of the fluid domain to minimize reflection of energy back into the system. Finally, the contacting surfaces of the strut and fluid domain were constrained with a kinematic boundary condition.

Representing the fluid domain as an acoustic medium required the assumptions of inviscid and irrotational flow, as well as linear fluid compressibility. These assumptions lead to an equilibrium equation resembling,

$$\partial p/\partial \boldsymbol{x} + \rho_f \ddot{\boldsymbol{u}}_f = 0, \tag{11}$$

where ρ_f is the fluid density, $\boldsymbol{x}$ is the nodal displacement vector, p is the fluid pressure and $\ddot{\boldsymbol{u}}_f$ is the fluid nodal acceleration vector. The constitutive behavior of acoustic fluid is,

$$p = -K_f \boldsymbol{\nabla} \cdot \boldsymbol{u}_f \tag{12}$$

where K_f is the bulk modulus of the fluid, $\boldsymbol{\nabla}$ is the gradient vector operator, and $\boldsymbol{u}_f$ is the fluid nodal displacement vector.

The generalized finite element equation of motion in the frequency domain for a free vibration problem without damping can be expressed as,

$$\begin{bmatrix} K_s & S_{fs}^T \\ 0 & K_f \end{bmatrix} \begin{Bmatrix} \boldsymbol{u} \\ p \end{Bmatrix} - \omega^2 \begin{bmatrix} M_s & 0 \\ -S_{fs} & M_f \end{bmatrix} \begin{Bmatrix} \boldsymbol{u} \\ p \end{Bmatrix} = 0 \tag{13}$$

where K_s and K_f are the structure and fluid stiffness, respectively, S_{fs} represents the fluid-structure interaction term through enforcing the kinematic and dynamic conditions at the fluid-solid interface, and M_s and M_f are the structure and fluid added mass, respectively. u describes the displacement of the structure and the p describes the pressure throughout the acoustic medium. EQ 13 can be symmetrized and solved iteratively to yield eigenvalues (ω^2), and eigenvectors ($\boldsymbol{\Phi}$). This method does not yield explicit values of the added mass acting on the structure but it does provide an indirect method by which to infer the effects of fluid and cavity interactions on the frequencies and shape of the resonant modes.

In the current simulations, the air above the free surface was not modeled. Work by [10] showed that the low density and high compressibility of air led to a negligible difference between simulations with and without acoustically-modeled air domains. Hence, fluid above the free surface was neglected to significantly decrease the computational cost.

2. RESULTS AND DISCUSSION

2.1 Numerically Predicted Mode Shapes

Mode shapes were identified using the eigen-analysis of the FEM model. The naming convention used throughout the discussion is: *[Primary axis] - [Motion type] - [# Node lines]*. For example, the first mode (X-Bend-1) is primarily bending about the X-axis with a single node line. The first five ordered mode shapes for the struts in air are shown in Figure 8. Higher-order X-bending modes (X-Bend-2 and X-Bend-3) demonstrate some twisting about the Z-axis induced by the chordwise asymmetry of the section shape. Note that the mode shapes shown are indentical for both struts and in any homogenous fluid (i.e. in-air or fully-submerged in water).

2.2 Experimentally Estimated Mode Shapes

The measured operating deflection shapes (ODSs) and corresponding resonant frequencies (f^*) of the PVC strut are shown in Figure 9. The rows correspond to values of the immersion ratio AR_h, and the columns are ordered from left to right by ascending resonant frequencies within each row. Note that the Y-Bend-1 mode (also known as the “lead-lag" mode) is not captured in the experiments because the half-bridges installed on the interior spars reject axial strains. The X-Bend-1 and X-Bend-3 modes are clearly represented in the ODSs. As the immersion depth is increased, these modes appear to change only slightly (some induced twist appears in the X-Bend-3 mode), but remain recognizable. The X-Bend-2 and Z-Twist-1 modes, however, are located relatively close to one another in the frequency domain, and both underlying normal modes contribute to the ODS at nearby frequencies. As a result, the underlying modes cannot be extricated from the ODS; rather, the ODS must be regarded as weighted blend of the underlying modes. As the immersion depth is increased to $AR_h = 0.5$, the second and third resonant modes become so closely-coupled (less than 2 Hz of separation), that the ODSs are almost indistinguishable. At $AR_h = 1.0$, the second and third resonant ODSs are re-ordered, relative to the dry ordering, such that Z-Twist-1 actually occurs at a slightly lower frequency than does X-Bend-2. At $AR_h = 1.5$, the original order is restored. Resonant mode shapes predicted by FEM for the cases where re-ordering occurs are shown at the bottom of the figure, corroborating the result of mode re-ordering.

2.3 Effects of Partial-Immersion on Resonance

Figure 10 depicts a comparison between the numerical and experimental resonant frequencies for both struts. The resonant frequencies of the aluminum and PVC struts are respectively shown in Figure 10a and Figure 10b. The resonance frequencies, nondimensionalized by the dry modal frequencies, $f_i^*/f_{i,dry}^*$ are shown for the aluminum and PVC struts in Figure 10c and Figure 10d, respectively. In the case of the aluminum strut, experimental data are available for the first three modes (X-Bend-1, X-Bend-2, and Z-Twist-3). For the PVC strut, experimental data are available for all of the modes pictured in the Figure 8 except Y-Bend-1.

The agreement between the numerical results and the experiments are good in most cases. A notable exception is the X-Bend-2 mode of the aluminum strut, where the FEM-predicted frequencies are consistently higher than the experimentally-observed ones. A likely explanation for the

discrepancy is the root boundary condition. In the FEM model, the root of the strut was perfectly clamped, while the experimental setup may have been influenced by the compliance of the load cell, reducing the stiffness of the system. The large curvature at the root in the X-Bend-2 mode induces a large bending moment at the root, which would exacerbate the issue of an imperfect clamp. The numerical and experimental results are in close agreement for the remaining resonant modes, both for the aluminum and for the PVC struts.

In general, with increasing immersion-ratio, the resonant frequencies in Figure 10a and Figure 10b decrease, with the exception of the Y-Bend-1 mode. As Figure 10c and Figure 10d demonstrate, the reduction is more-severe for the PVC strut than the aluminum strut. Both effects are attributed to the inertial resistance of the water to the strut's motion. Added mass is the integrated inertial resistance to the local accelerations of the body, which as the name implies, may be modeled by additional mass distributed on the structure. The distribution of the added mass is purely a function of the body's motion (if free-surface waves are neglected). The resonant frequencies of the PVC strut are more-strongly reduced than the aluminum resonant frequencies because the solid-to-fluid density ratio is much smaller in the case of the PVC strut. For similar mode shapes, the fluid added mass will be nearly identical for the two struts, but will make up a greater percentage of the total system mass in the case of the PVC strut. As a result, the lighter structure is influenced to a much greater degree by the immersion into a dense fluid.

Mode shapes where deflection occurs in a direction with a large projected area (e.g. X-Bend-1) are necessarily more-strongly affected by the surrounding fluid's added mass than are mode shapes that present minimal projected area in the direction of primary motion (Y-Bend-1). This is demonstrated in Figure 10c and Figure 10d by the fact that, as the struts are immersed, the reductions to the resonant frequencies are not uniform. Namely, the first-order resonant modes (X-Bend-1 and Z-Twist-1) are affected more-severely than the higher-order modes. Moreover, note that inflections occur in the resonant frequencies of the higher-order modes. This occurs when a nodal line of the respective resonant mode is submerged. Motion along the node lines is identically zero, and so induces very little acceleration in the surrounding fluid; the result is a near-zero change in the hydrodynamic added mass.

As observed in the preceding section, the second and third modes approach one another (frequency coalescence) between $AR_h = 0.5$ and $AR_h = 1.5$. This occurs because the node line of the X-Bend-2 becomes submerged at approximately $AR_h = 1$, causing the added mass component to plateau. The added mass effect is proportionally severe enough to cause a re-ordering of modes at AR_h only in the case of the PVC strut. With the aluminum strut, the modes coalesce but do not re-order. Frequency coalescence is a practical concern because it signifies the sharing of energy between two modes; in extreme cases, one mode can feed energy into another in an unbounded fashion, resulting in a dynamic instability known as flutter, which can cause accelerated fatigue and/or catastrophic structural failure.

2.4 Effects of Ventilation

The dashed lines in figs 10 denote the numerical resonant frequencies when the air-filled cavity (Figure 7b) was included in the fluid domain. In all cases, the resonance frequencies increase from their fully-wetted values. In the fully-ventilated configuration, nearly half of the previously-wetted area is surrounded by air, which presents a negligible inertial opposition to motion, thus reducing the added mass. As a result, the resonant frequencies increase to a value somewhere between those in the corresponding fully-wetted condition and the dry condition.

CONCLUSIONS

Experimental and numerical investigations of the resonant behavior of aluminum and PVC struts partially immersed in water have been conducted. A simple shape-sensing methodology has been developed around an aluminum spar instrumented with strain gauges, which permits bending and twisting deformations of the PVC strut to be inferred with good accuracy. The close agreement between experimental and numerical resonant modes and frequencies validate the accuracy of the FEM model, which uses acoustic elements to simulate the air/water fluid domain.

Partial immersion in water causes the resonant frequencies of both struts to decrease, though the effect is more pronounced for the PVC strut because hydrodynamic added mass makes up a greater proportion of the effective system mass. The modal-dependence of the fluid added mass causes the second bending and first twisting frequencies to approach one another for the aluminum strut and to change order for the PVC strut. The re-ordering of modes has been shown by the numerical mode shapes and by the operating deflection shapes (ODSs) measured in the experiments. This frequency coalescence leads to concerns about coupled dynamic instability (flutter) during operation. The formation of a fully-ventilated (FV) cavity causes the resonant frequencies to increase again, as air replaces some of the water surrounding the strut, reducing the fluid added-mass.

Future Work

Future experiments will focus on the creation of single/multi-input-multi-output (SIMO/MIMO) frequency response functions matrix. An electrodynamic shaker will be used to excite the strut in in FW and FV flow conditions. It is hoped that from these data, quantitative values of modal added mass and damping, as well as improved estimates of mode shapes, will be inferred.

ACKNOWLEDGMENTS

This material is based upon work supported by the National Science Foundation Graduate Student Research Fellowship under Grant No. DGE 1256260.

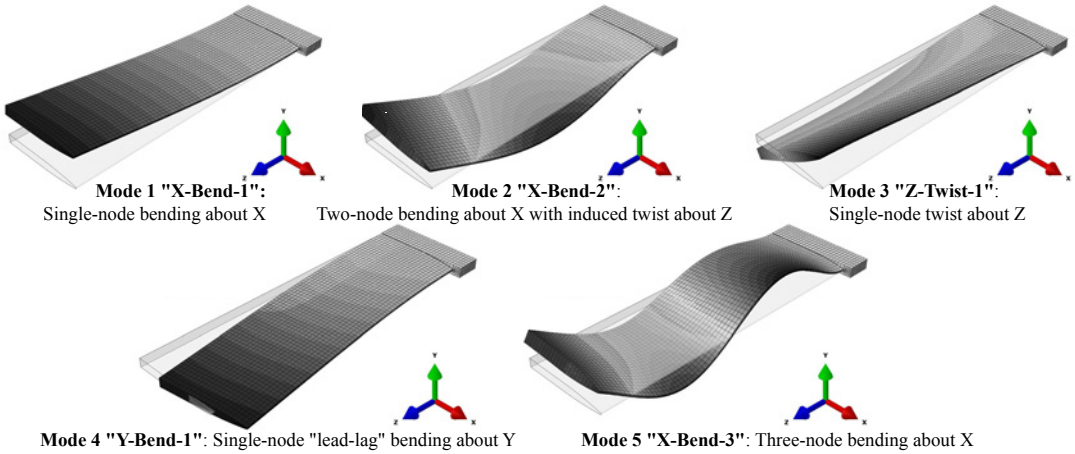

Figure 8. The first five dry ($AR_h = 0$) mode shapes identified by FEM (identical for PVC and aluminum struts).

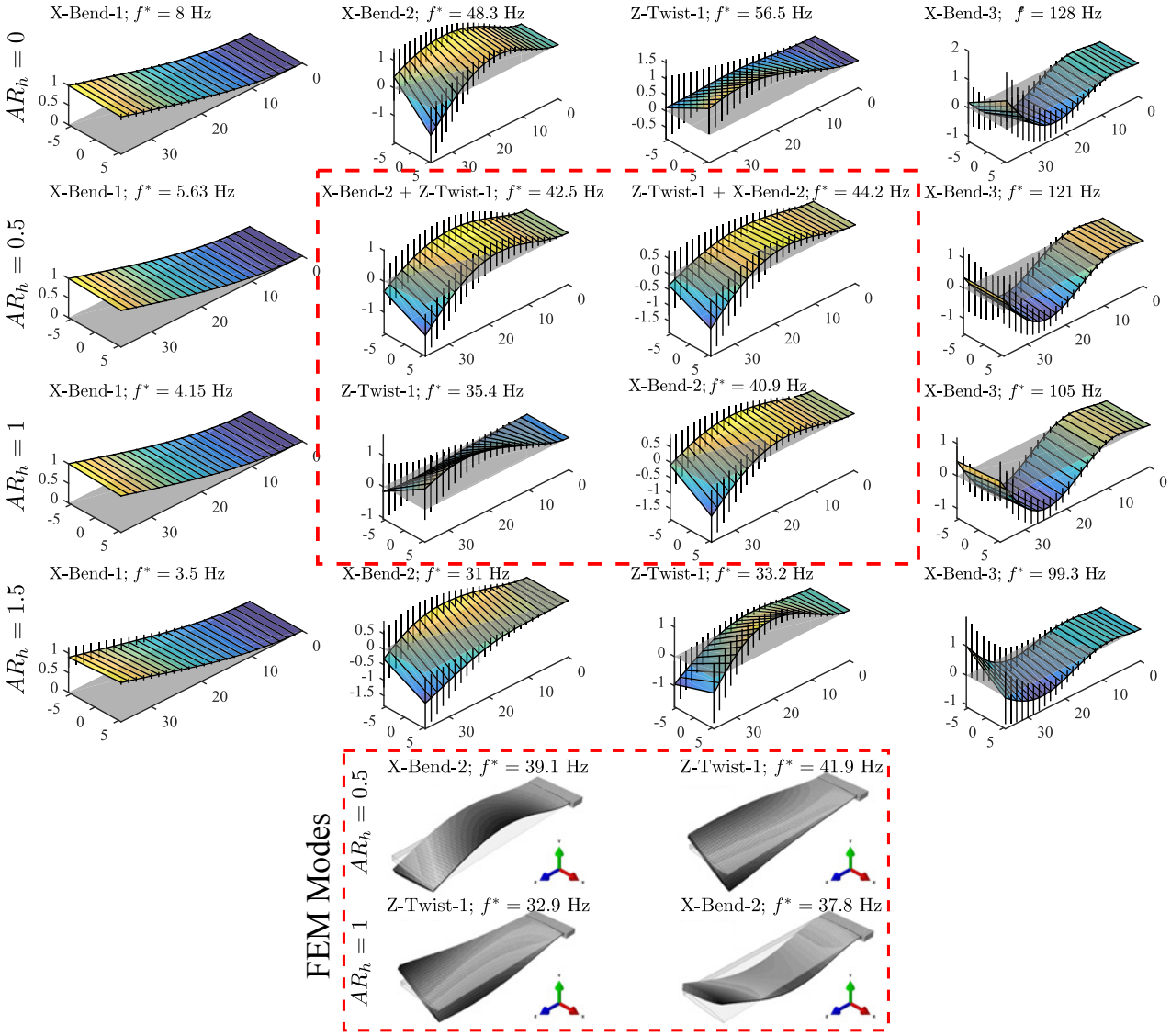

Figure 9. Resonant Operating Deflection Shapes (ODSs) measured in experiments for the PVC strut. The undeformed surface is indicated by the grey patch. Vertical bars indicate ± one standard deviation in the ODS. The second and third resonant modes coalesce and "flip" order between $AR_h = 0.5$ and $AR_h = 1.0$. Numerically-predicted modes, shown at the bottom of the figure, also indicate a flipping of the second and third modes at $AR_h = 0.5$ and $AR_h = 1.0$.

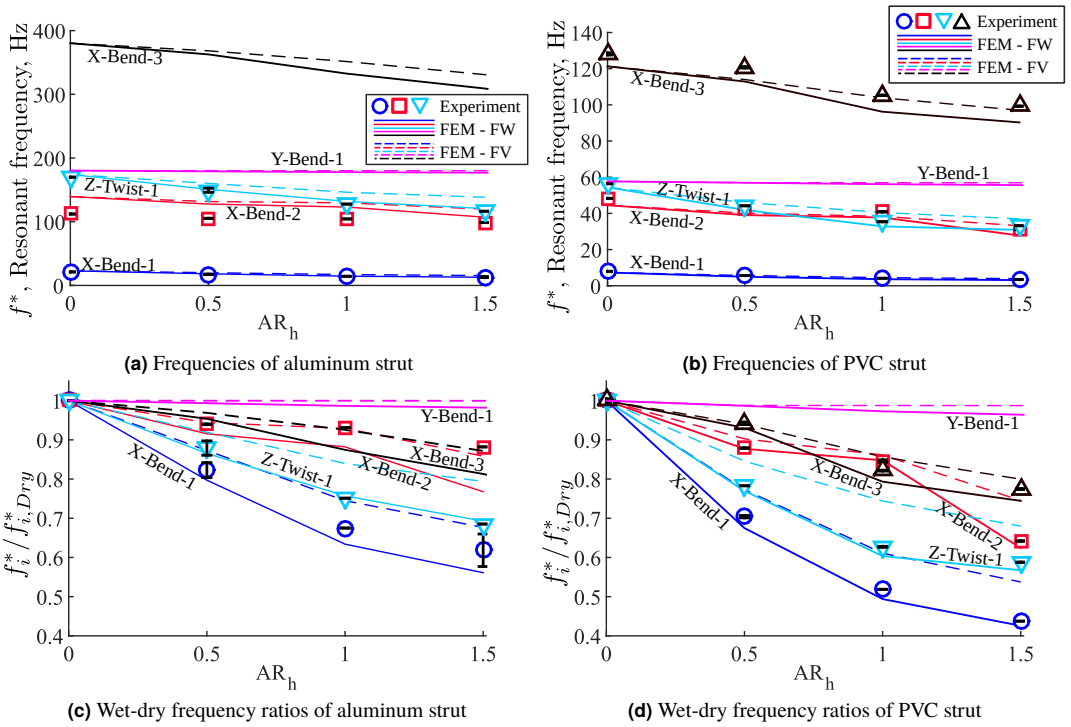

(a) Frequencies of aluminum strut

(b) Frequencies of PVC strut

(c) Wet-dry frequency ratios of aluminum strut

(d) Wet-dry frequency ratios of PVC strut

Figure 10. Dimensional resonant frequencies of **(a)** aluminum and **(b)** PVC struts and the wet-to-dry frequency ratios of **(c)** aluminum and **(d)** PVC struts with varying immersed aspect ratio. Symbols denote mean experimental resonant frequencies, with bars indicating ± one standard deviation. Solid lines indicate the FEM results with a fully-wetted fluid domain and dashed lines indicate the FEM results with a simulated fully-ventilated cavity.

REFERENCES

[1] E. J. Chae, D. T. Akcabay, and Y. L. Young. Dynamic response and stability of a flapping foil in a dense and viscous fluid. *Physics of Fluids*, 25(10), 2013.

[2] D. T. Akcabay and Y. L. Young. Influence of cavitation on the hydroelastic stability of hydrofoils. *Journal of Fluids and Structures*, 49:170 – 185, 2014.

[3] D. T. Akcabay, E. J. Chae, Y. L. Young, A. Ducoin, and J. A. Astolfi. Cavity induced vibration of flexible hydrofoils. *Journal of Fluids and Structures*, 49:463 – 484, 2014.

[4] D. T. Akcabay and Y. L. Young. Parametric excitations and lock-in of flexible hydrofoils in two-phase flows. *Journal of Fluids and Structures*, 57:344 – 356, 2015.

[5] J. P. Breslin and R. Skalak. Exploratory study of ventilated flows about yawed surface-piercing struts. Technical Report 2-23-59W, NASA Tech. Mem., Washington, DC, USA, 1959.

[6] R. S. Rothblum, D. A. Mayer, and G. M. Wilburn. Ventilation, cavitation and other characteristics of high speed surface-piercing strut. Technical Report 3023, Department of the Navy- Naval Ship Research and Development Center, Washington DC, July 1969.

[7] C. M. Harwood, K. A. Brucker, F. Miguel, Y. L. Young, and S. L. Ceccio. Experimental and numerical investigation of ventilation inception and washout mechanisms of a surface-piercing hydrofoil. In *Proceedings of the 30th Symposium on Naval Hydrodynamics*, Hobart, Tasmania, November 2014. In Press.

[8] C. M. Harwood, Y. L. Young, and S. L. Ceccio. Ventilated cavities on a surface-piercing hydrofoil at moderate froude numbers: cavity formation, elimination, and stability. *Journal of Fluid Mechanics*, 2015. MANUSCRIPT UNDER REVIEW.

[9] Y. Fu and W. G. Price. Interactions between a partially or totally immersed vibrating cantilever plate and the surrounding fluid. *Journal of Sound and Vibrations*, 118(3):495–513, 1987.

[10] M. R. Kramer, Z. Liu, and Y. L. Young. Free vibration of a cantilevered composite plate in air and in water. *Journal of Composite Structures*, 95:254.263, 2013.

[11] U. S. Lindholm, D. D. Kana, W. H. Chu, and H. N. Abramson. Elastic vibration characteristics of cantilever plates in water. *Journal of Ship Research*, 9:11–22, 1965.

[12] M. R. Motley, M. R. Kramer, and Y. L. Young. Free surface and solid boundary effects on the free vibration of cantilevered composite plates. *Journal of Composite Strucutres*, 96:365–375, 2013.

[13] B. J. Schwarz and M. H. Richardson. Experimental modal analysis. In *CSI Reliability week*, volume 35, pages 1–12. Orlando FL, 1999.

[14] Dassault Systèmes Simulia Corp, 1080 Main Street, Pawtucket, RI, 02860. *Abaqus Analysis User's Manual Ver. 6.12*, 2012.